J Membrane Biol (2014) 247:395–408
DOI 10.1007/s00232-014-9646-z

# Continuum Approaches to Understanding Ion and Peptide Interactions with the Membrane

**Naomi R. Latorraca · Keith M. Callenberg · Jon P. Boyle · Michael Grabe**

Received: 12 October 2013 / Accepted: 22 February 2014 / Published online: 21 March 2014


**Abstract** Experimental and computational studies have shown that cellular membranes deform to stabilize the inclusion of transmembrane (TM) proteins harboring charge. Recent analysis suggests that membrane bending helps to expose charged and polar residues to the aqueous environment and polar head groups. We previously used elasticity theory to identify membrane distortions that minimize the insertion of charged TM peptides into the membrane. Here, we extend our work by showing that it also provides a novel, computationally efficient method for exploring the energetics of ion and small peptide penetration into membranes. First, we show that the continuum method accurately reproduces energy profiles and membrane shapes generated from molecular simulations of bare ion permeation at a fraction of the computational cost. Next, we demonstrate that the dependence of the ion insertion energy on the membrane thickness arises primarily from the elastic properties of the membrane. Moreover, the continuum model readily provides a free energy decomposition into components not easily determined from molecular dynamics. Finally, we show that the energetics of membrane deformation strongly depend on membrane patch size both for ions and peptides. This dependence is particularly strong for peptides based on simulations of a known amphipathic, membrane binding peptide from the human pathogen *Toxoplasma gondii*. In total, we address shortcomings and advantages that arise from using a variety of computational methods in distinct biological contexts.

**Keywords** Ion permeation · Membrane elasticity · Continuum · Coarse grained · Rhoptry protein 5 (ROP5)

Naomi R. Latorraca and Keith M. Callenberg have contributed equally to this work.

N. R. Latorraca · J. P. Boyle · M. Grabe (✉)
Department of Biological Sciences, University of Pittsburgh, 4249 Fifth Avenue, Pittsburgh, PA 15260, USA
e-mail: michael.grabe@ucsf.edu

K. M. Callenberg
Carnegie Mellon University-University of Pittsburgh Ph.D. Program in Computational Biology, 4249 Fifth Avenue, Pittsburgh, PA 15260, USA

M. Grabe
Department of Computational & Systems Biology, University of Pittsburgh, 3501 Fifth Avenue, Pittsburgh, PA 15260, USA

M. Grabe
Department of Pharmaceutical Chemistry, Cardiovascular Research Institute, University of California, San Francisco, 555 Mission Bay Blvd South, San Francisco, CA 94158, USA

## Introduction

The cell membrane serves as a critical barrier differentiating the interior of the cell from the extracellular medium. It is inextricably linked to cellular identity—without a membrane, a cell cannot control its internal chemistry. Loss of membrane integrity often leads to cell death, and organisms have evolved strategies to kill other cells by attacking their membranes, as in the mechanisms of many antibiotics. Strikingly, cells induce their own deaths by compromising the integrity of their membranes during apoptosis through decoupling the cytoskeletal network from the membrane, which leads to blebbing (Mills et al. 1998).

Chemical and physical principles underlie the membrane's dual role as a barrier to the external environment and regulator of nutrient transport into and out of the cell.

Packed hydrophobic lipids form a low-dielectric barrier to charged and polar molecules, while membrane-spanning channels and pumps exert control over the passage of ions and macromolecules. Such transmembrane (TM) proteins typically consist of hydrophobic amino acids that are energetically stabilized in the low-dielectric membrane. However, proteins with functionally important, highly charged moieties also reside in the hydrophobic bilayer core, suggesting that some mechanism must exist to mitigate the electrostatic cost of their insertion. In particular, in vitro translocation experiments suggest that TM segments harboring a central, charged residue partition into the bilayer at a small energetic cost of only 2–3 kcal/mol (Hessa et al. 2005). Recent molecular dynamics (MD) simulations have demonstrated that an arginine residue positioned in the bilayer core may "snorkel", bringing water and ions into the bilayer to interact favorably with the buried amino acid, incurring an energy penalty associated with membrane rearrangement (MacCallum et al. 2007; Dorairaj and Allen 2007). Membrane deformations and distortions, therefore, represent a potential mechanism for charge insertion into the bilayer.

Membrane elasticity likely facilitates a range of biological processes, from the large-scale deformations required for vesicle budding and fusion to the localized permeation of small molecules across bilayers. Carrier-mediated ion transport and bare ion permeation constitute two distinct contexts in which to further investigate how membrane bending modulates membrane transport phenomena. For example, ionophores such as *Streptomyces*-derived valinomycin selectively chelate potassium ions and shuttle them across host cell bilayers, disrupting their electrochemical gradient. Similarly, the threat of bare permeation of small ions and water molecules to high-fidelity nucleic acid replication might have spurred the development of the phospholipid bilayer as an early and critical evolutionary adaptation on the molecular level (Mansy and Szostak 2008; Budin and Szostak 2011). Nonetheless, bare ion permeation, while rare, does occur, although its mechanism remains disputed in the literature.

At present, ion permeation is thought to occur via two distinct mechanisms: solubility-diffusion and transient pore formation (Paula et al. 1996, 1998; Marrink et al. 2009). In the former, the ion must partition into the hydrophobic core, surmounting a considerable energy barrier, diffuse across the core, and resolvate as it exits the opposite membrane leaflet (Dilger et al. 1979; Finkelstein 1987). However, rates for bare ion permeation predicted from solubility-diffusion theory disagree with experiment by several orders of magnitude (Parsegian 1969). Paula et al. (1996, 1998) investigated how potassium permeation depends on bilayer thickness and found that crossing rates for thin bilayers are best understood by transient pore formation, while crossing rates for thick bilayers are explained by the solubility-diffusion model. Further support for the transient pore model comes from simulation, where studies have demonstrated that electroporation, membrane tension, or the presence of anti-microbial peptides all induce hydrophilic, transient pores, which serve as pathways for ions, lipids and other small molecules (Kandasamy and Larson 2006; Tieleman and Marrink 2006; Marrink et al. 2009; Bennett and Tieleman 2011). In these studies, the primary barrier to permeation is the cost of creating a toroidal pore in the membrane. A third theory, closely related to transient pore formation, suggests that charged molecules at the membrane surface induce the formation of water-head group defects that penetrate deep into the membrane, allowing for the permeation of charges and water molecules through a temporary, electrostatically-favorable environment (Tepper and Voth 2006; Khavrutskii et al. 2009; Li et al. 2012).

While there have been previous studies that have used analytic and continuum approaches to understand bare ion permeation (Parsegian 1969; Finkelstein 1987; Paula et al. 1996, 1998), more recent attempts to compare continuum approaches with detailed MD simulations suggest a failure in the continuum methods (Li et al. 2012). We believe that this failure is largely due to the inability of most continuum implementations to account for the deformable nature of the membrane. Recently, we developed a method that overcomes this shortcoming by using elasticity theory to predict membrane distortions around TM proteins harboring charged, buried residues (Choe et al. 2008; Callenberg et al. 2012). Bending drastically reduces the energy required to insert these proteins into the membrane, and our model is in quantitative agreement with results from atomistic MD simulations, but requires a fraction of the computational cost. To date, we have only assessed the model's ability to predict the static configurations and stability of embedded membrane proteins, but here, we extend our work by considering the penetration of ions and peptides into the membrane from solution. We show that membrane flexibility largely reconciles previous discrepancies between MD simulations and continuum calculations. Snapshots from coarse-grained MD simulations of ion penetration are compared with snapshots from the continuum model, revealing the importance of system size in providing qualitative agreement between different approaches. Additionally, our model produces very similar free energy profiles to all-atom MD simulations of charged groups moving into bilayers of different thickness (Li et al. 2012). A free energy decomposition, which is easily performed with our approach, reveals that the increase in energy required to penetrate thick bilayers is almost entirely due to the increased bilayer bending energy. Finally, we use coarse-grained simulations of peptide association with the membrane to show that computed free

energy profiles depend heavily on the system size, as revealed by our ion penetration studies.

## Methods

### Description of the Continuum Model

Previously, we developed a continuum membrane model and search algorithm to calculate insertion energies and membrane distortions for single pass TM proteins (Choe et al. 2008; Callenberg et al. 2012). Briefly, in our model the total energetic stability of the solute in the membrane, $\Delta G_{\text{total}}$, is approximated by the following equation:

$$\Delta G_{\text{total}} = \Delta G_{\text{mem}} + \Delta G_{\text{elec}} + \Delta G_{\text{np}}, \tag{1}$$

where the first term on the right hand side ($\Delta G_{\text{mem}}$) is the energy associated with distortions in the membrane caused by embedding the solute, the second term ($\Delta G_{\text{elec}}$) is the electrostatic cost required to move the charged solute from solution into the low-dielectric environment of the membrane, and the final term ($\Delta G_{\text{np}}$) is the nonpolar or hydrophobic energy gained by removing portions of the solute surface from water and burying them in the membrane. All energies are calculated with respect to the molecule free in solution far from an unstressed membrane; therefore, negative values indicate stabilization in the membrane. This model is in excellent agreement with free energies calculated from simulations (Choe et al. 2008), and the model supports experimental observations on the stability of voltage sensors from voltage-gated potassium channels (Callenberg et al. 2012).

All of the energies presented in this manuscript are equilibrium values calculated from static configurations. The exact computational details closely follow the procedure outlined in our previous manuscript (Callenberg et al. 2012) and additional details can be found in Choe et al. (2008). Briefly, the energetic terms and procedure are calculated as follows.

#### *Membrane Deformation Energy ($\Delta G_{mem}$)*

We use linear elasticity theory to determine the shape and energetic cost of deforming the bilayer at the site of ion penetration. Specifically, we use a modified Helfrich Hamiltonian, which includes terms for membrane bending, compression and tension (de Gennes 1969; Helfrich 1973; Harroun et al. 1999):

$$\Delta G_{\text{mem}} = \frac{1}{2}\int_{\Omega}\left[\frac{K_{\text{a}}}{L_0^2}(u^- - u^+)^2 + \frac{K_{\text{c}}}{2}\left(\left(\nabla^2 u^-\right)^2 + \left(\nabla^2 u^+\right)^2\right) + \frac{\alpha}{2}\left((\nabla u^-)^2 + (\nabla u^+)^2\right)\right]\mathrm{d}x\mathrm{d}y, \tag{2}$$

where $u^+$ is the shape of the upper leaflet and $u^-$ is the shape of the lower leaflet, $L_0$ is the equilibrium thickness of the membrane, $K_{\text{a}}$ is the compression modulus, $K_{\text{c}}$ is the membrane bending modulus, and $\alpha$ is the surface tension. The surfaces are represented in the Monge gauge, and correspondingly, the integral extends over the entire $x$–$y$ domain, $\Omega$. The functional derivative of Eq. 2 with respect to variations in $u^+$ and $u^-$ gives the following partial differential equations (PDEs) that determine the shapes of each leaflet:

$$\begin{aligned}\nabla^4 u^+ - \frac{\alpha}{K_{\text{c}}}\nabla^2 u^+ + \frac{2K_{\text{a}}}{K_{\text{c}}L_0^2}(u^+ - u^-) = 0,\\ \nabla^4 u^- - \frac{\alpha}{K_{\text{c}}}\nabla^2 u^- + \frac{2K_{\text{a}}}{K_{\text{c}}L_0^2}(u^- - u^+) = 0.\end{aligned} \tag{3}$$

The last term on the left hand side of each equation couples the upper and lower leaflets. Thus, Eq. 3 is the set of equations that result from minimizing Eq. 2 for a given set of boundary conditions. To minimize the total energy of the system, we employ Powell's method to identify the optimal boundary condition for Eq. 3 that produce the membrane shape that minimizes all of the energy terms shown in Eq. 1. More specifically, the coupled set of fourth-order equations requires two boundary conditions to be specified on the inner boundary, where the bilayer contacts the ion, and at the outer boundary, far from the ion. We assume that the membrane is flat at its equilibrium thickness, $L_0$, far from the ion. At the ion, we impose a radially symmetric contact height for the upper and lower leaflets, and we impose contact angles that determine the slope, or curvature, of the membrane as it meets the ion (Fig. 1). Thus, four independent parameters determine the boundary conditions at the inner boundary. We determined these values by carrying out a search on all four parameters to find the membrane shapes that minimize the total energy in Eq. 1 as discussed in reference (Callenberg et al. 2012). In some cases described in the "Results" section, we optimized only the contact angle of the leaflet undergoing ion penetration and imposed a contact angle of zero on the opposite leaflet. The PDEs in Eq. 3 were solved using a second-order finite difference method written in radial coordinates ($r$ and $\theta$), and the membrane bending energy was determined by using a second-order scheme to compute the integral in Eq. 2. While the solver is a general 2D solver, the solutions for the ion–membrane systems described in this paper only vary in $r$, not $\theta$, due to the underlying symmetry of the system and could have been represented with a 1D solver. However, we can also use the 2D solver to address more complex problems that lack radial symmetry, and it is highly accurate and fast compared to the electrostatics calculations performed here. All code was written in Matlab (The MathWorks, Inc., Natick, MA).

*Electrostatic Energy ($\Delta G_{elec}$)*

We solve the non-linear Poisson–Boltzmann equation to determine the cost of inserting a charged molecule into a neutral, uncharged bilayer:

$$-\nabla \cdot [\epsilon(\boldsymbol{r})\nabla\phi(\boldsymbol{r})] + \kappa^2(\boldsymbol{r})\sinh[\phi(\boldsymbol{r})] = \frac{e}{k_B T}4\pi\rho(\boldsymbol{r}), \qquad (4)$$

where $\phi(\boldsymbol{r}) = \Phi(\boldsymbol{r})/k_B T$ is the reduced electrostatic potential at position $\boldsymbol{r}$, $\kappa$ is the Debye–Huckel screening coefficient to account for ionic shielding, $\varepsilon$ is the spatially-dependent dielectric constant, $e$ is the electron charge and $\rho$ is the charge density within the protein. The electrostatic potential is solved using the software APBS (Baker et al. 2001) along with scripts for including the dielectric influence of the membrane similar to those found in APBSmem (Callenberg et al. 2010). The electrostatic energy of the ion in the membrane compared to solution, $\Delta G_{\text{elec}}$, is calculated by subtracting the total energy of the molecule in the membrane from the value in solution, far from the membrane. This energy is usually referred to as the Born solvation energy, $\Delta G_{\text{Born}}$.

In a separate electrostatics calculation, we include the influence of the membrane dipole potential by adding a sheet of dipole charges at the interface between the head group and the hydrocarbon core, one sheet for the upper leaflet and one for the lower leaflet. This term accounts for the large electrostatic role that the membrane dipole plays in charge permeation events, and we tune the charges and the separation distance of the dipoles to achieve +300 mV at the center of the membrane, which is estimated for phosphatidylcholine (PC) bilayers (Wang et al. 2006). For this calculation, we solve the linearized form of the Poisson–Boltzmann equation to expedite the calculations. First, we calculate the total electrostatic energy of the charged molecule in the bilayer with the dipole potential on. Next, we subtract off the "self" dipole energies by turning off the charge on the permeating molecule and re-performing the calculation with the dipole charges still on. Finally, we subtract the electrostatic energy of the charged molecule with the dipole potential turned off. These three terms added in this way provide the interaction energy between the ion and the membrane dipole potential, $\Delta G_{\text{dipole}}$. Care was taken to avoid double counting of charge–charge interactions. The total electrostatic energy is then given by the sum of the Born solvation energy and the dipole energy: $\Delta G_{\text{elec}} = \Delta G_{\text{Born}} + \Delta G_{\text{dipole}}$. We found that including the dipole in the electrostatics calculation throughout the search, rather than as a separate calculation, only resulted in less than a 1 kcal/mol difference in the final energy for all membrane configurations, with the exception of the DSPC-like continuum bilayer configurations at $z = -1$ and 0 Å from bilayer center, which resulted in a 1.5 kcal/mol difference.

*Nonpolar Energy ($\Delta G_{np}$)*

The nonpolar energy arises from the tendency of water to exclude molecules, resulting in the clustering of hydrophobic proteins and the stabilization of molecules in the membrane. We model the nonpolar energy, $\Delta G_{\text{np}}$, as proportional to the difference in the ion's solvent accessible surface area (SASA) in the membrane compared to solution:

$$\Delta G_{\text{np}} = a \cdot (A_{\text{mem}} - A_{\text{sol}}), \qquad (5)$$

where $A_{\text{mem}}$ is the ion SASA in the membrane, $A_{\text{sol}}$ is the total ion SASA, and $a = 0.028$ (kcal/mol)/Å$^2$. The constant $a$ was determined based on the partitioning of small nonpolar molecules between aqueous and organic phases (Sitkoff et al. 1994). SASA values are calculated with a modified Shrake–Rupley algorithm (1973) using the solvent-accessible surface representation of the ion with a water probe radius of 1.4 Å. In the presence of the membrane, if the point on the surface of the ion lies between the upper, $u^+$ and lower, $u^-$, leaflets then it is considered occluded and does not contribute to $A_{\text{mem}}$. Matlab's cubic interpolation function was used to navigate between the position of the point on the ion surface and the grid points describing the upper and lower membrane surfaces.

*Minimizing the Total Energy*

To simulate the permeation of an ion, we systematically translated the molecule in steps of 1 Å along an axis orthogonal to the membrane normal, which we call the $z$ axis. For each position, we carried out a search using Powell's method (1964) to determine the deformation that minimized the total energy of the system in Eq. 1. Initially, during the search, the contact height of the upper and lower leaflets as well as the slope of membrane contact with the ion were varied (Fig. 1b). To facilitate convergence of the search, we used the final, optimal membrane configuration from one calculation as the starting guess for the subsequent position along the pathway.

Continuum Setup and Parameters

We created input files containing radii and charge for the potassium ion and chloride ion calculations, assigning them their respective charges of +1 and −1, and we used unhydrated ionic radii, 1.39 Å for $K^+$ and 1.81 Å for $Cl^-$ (Shannon 1976). We also specified $r_0$, the radius of the solute inclusion. See Fig. 1 for an illustration of the geometry of the system. For $K^+$ and $Cl^-$, we have no way to determine the extent of ion hydration as it permeates the membrane. Thus, for $K^+$, we treat $r_0$ as equivalent to the SASA radius. We then set the $r_0$ for $Cl^-$ equal to $r_0$ for $K^+$ but recognize that even slight increases in $r_0$ lower the cost of ion insertion into the membrane (data not shown).

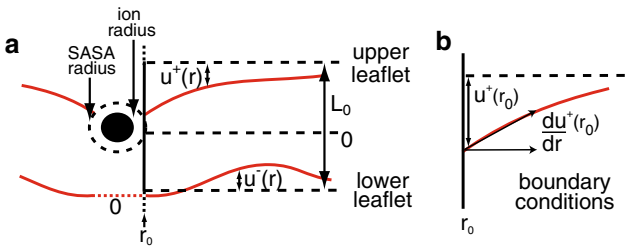


**Fig. 1** Geometry of the system in the continuum model. **a** Cross section showing membrane distortions in the upper and lower leaflets. *Solid red lines* indicate the membrane–water interfaces. *Dashed black lines* indicate the equilibrium heights of the membrane leaflets and the midplane at $z = 0$. $u^+$ and $u^-$ represent the displacement from equilibrium for the upper and lower leaflets, respectively. The equilibrium bilayer thickness is $L_0$. The inner boundary conditions are applied at $r_0$, where the solvent accessible surface area (SASA) of the ion contacts the membrane. **b** The contact point $u^+(r_0)$ is determined from the search angle that minimizes the total energy Eq. 1. The ion–membrane contact angle, $du^+/dr$, is a free parameter in the model that is optimized during energy minimization. The contact point and angle on the lower leaflet are treated in similar manners (Color figure online)

To capture the effect of increasing bilayer thickness on ion permeation in our continuum model, we also considered how lipid alkyl tail length, a variable in MD simulations and experiments, corresponds to bilayer thickness, and how this in turn affects the elastic properties of the bilayer. Several groups have shown that increasing hydrocarbon chain length leads to a linear increase in bilayer thickness and that the bending modulus, $K_c$ increases systematically as lipid chain length increases (Lewis and Engelman 1983; Rawicz et al. 2000). However, the compression modulus, $K_a$, does not vary significantly between different lipid chain lengths. We therefore used empirical data to add lipid-specific information to our continuum model while maintaining its computational efficiency. Rawicz and co-workers developed an empirical relation to describe the hydrophobic thickness to $K_a$ and $K_c$:

$$K_c = \frac{L_c^2}{24} K_a, \tag{6}$$

where 24 is an empirical constant and $L_c$ is the equilibrium hydrocarbon thickness, which is equal to the entire bilayer thickness, $L_0$, minus twice the thickness of the head group region. For all calculations, we used 8 Å as the head group thickness (Helm et al. 1987). We computed $K_c$ from an average $K_a$ of 230 mN/m (Rawicz et al. 2000) and from hydrophobic thicknesses of simulated PC bilayers reported by Li et al. (2012), with the exception of DSPC. For the hydrophobic thickness of DSPC, which was simulated at a higher temperature than the other lipid types, we calculated the average increase in hydrophobic thickness among the other bilayers and added this value to the thickness of DPPC.

**Table 1** Parameters for all continuum calculations

| Parameters | Values |
|---|---|
| Electrostatics grid dimensions | 161 × 161 × 161 Å$^3$ |
| Coarse grid lengths | 200 × 200 × 200 Å$^3$ |
| Fine grid lengths | 50 × 50 × 50 Å$^3$ |
| Radial points | 1,400 |
| Counter-ions | 0.1 M symmetric salt |
| Protein dielectric | 2.0 |
| Membrane dielectric | 2.0 |
| Head group dielectric | 80.0 |
| Solvent dielectric | 80.0 |
| Solvent probe radius | 1.4 Å |
| Surface sphere density | 10.0 grid points/Å$^2$ |
| Temperature | 298.15 K |
| Membrane thickness | See Table 2 |
| Head group thickness | 8.0 Å |
| Bending modulus ($K_c$) | See Table 2 |
| Compression modulus ($K_a$) | 2.30 × 10$^{-11}$ N/Å |
| Surface tension ($\alpha$) | 3.00 × 10$^{-13}$ NÅ |
| Outer boundary radius | 800 or 19.5 Å |

We also had to select an outer radius parameter to use as the outer boundary for membrane deformations in the continuum model. In order to bring the sizes of the continuum and coarse-grained lipid patches into agreement, we chose an outer radius for the continuum model such that twice the radius equaled the length of one side of the coarse-grained lipid patch. Since the surface area taken up by individual lipids decreases slightly as tail length increases, we used lipid surface area values reported by Li and co-workers to estimate the outer radius that would provide equivalent surface area to that of a 48 PC lipid patch. Please see Tables 1 and 2 for continuum calculation parameters.

## Coarse-Grained Simulations and Free Energy Calculations

We performed coarse-grained MD simulations using GROMACS version 4.5.3 (Hess et al. 2008) and the MARTINI forcefield version 2.0 with polarizable water (Yesylevskyy et al. 2010). Following the protocols outlined by the Sansom Lab (Bond et al. 2008; Wee et al. 2011), umbrella sampling combined with weighted histogram analysis method (WHAM) were used to construct free energy profiles for peptide helices or permeating ions (Kumar et al. 1992). The $z$-position of the ion or center of mass (COM) of the helix were harmonically restrained with respect to the COM of the membrane, and this distance was chosen as the reaction coordinate. For cation simulations, $Na^+$ was used rather than $K^+$, which has not

**Table 2** Elastic membrane material properties

| Lipid types | Carbon atoms | $L_0$ (Å) | $K_c$ (NÅ) |
|---|---|---|---|
| DDPC | 10 | 32.0 | $2.5 \times 10^{-10}$ |
| DLPC | 12 | 36.3 | $4.0 \times 10^{-10}$ |
| DMPC | 14 | 39.9 | $5.5 \times 10^{-10}$ |
| DPPC | 16 | 43.6 | $7.0 \times 10^{-10}$ |
| DSPC | 18 | 47.7 | $5.9 \times 10^{-10}$ |

been parameterized in MARTINI. Meanwhile, $K^+$ was used in the continuum model due to the prevalence of $K^+$ permeation data in the literature. Ion/helix positions were sampled from one side of the membrane to the other in 1 Å steps. In each simulation, the ion/helix was initially placed at the restraint minimum in a pre-equilibrated bilayer. The membrane starts in a flat state that is identical across all simulations, and the protein is translated to many different starting positions across the bilayer prior to minimization and production runs (Fig. 5b). The long axis of the helix was initially parallel to the membrane normal with the N-terminus always pointing in the positive $z$ direction. Minimization and equilibration successfully removed steric clashes between the embedded ion/helix and the lipids. We could possibly have benefited from a speed up in convergence by using the final configuration from the previous ion position to initiate new simulations. However, we were also interested in the ability of the coarse-grained membrane to undergo large scale conformational changes in a limited time, so we initiated all simulations from a flat membrane, a universally accepted approach for molecular simulation. After energy minimization, MD was performed for 60 ns. The first 10 ns of each simulation were discarded as equilibration.

We used semi-isotropic pressure coupling with a Berendsen barostat (Berendsen et al. 1984) at 1 bar in $x$ and $y$ with a coupling of 1 ps and a compressibility of $3.0 \times 10^{-5}$. Particle mesh Ewald electrostatics were used with a 1 Å grid spacing. The software `g_wham` was used to calculate the potential of mean force (PMF) using WHAM (Hub et al. 2010; Kumar et al. 1992). Two hundred bins were used to construct the histogram, and the energy in bulk solution at ±30 Å was defined to be 0.

All coarse-grained simulations started from an identical pre-equilibrated DPPC bilayer composed of either 128 lipids and 2,000 waters or 512 lipids and 8,000 waters at 320 K. Ions were added as necessary to neutralize the system. The sequence of helix 2 from the arginine-rich amphipathic helix (RAH) domain of *Toxoplasma gondii* rhoptry protein 5 (ROP5) was obtained from the ToxoDB online resource (LRKRLAQHFRRLRGFFGR). An idealized alpha helix was created with this sequence using VMD Molefacture plugin version 1.2 (Humphrey et al. 1996). The secondary structure was harmonically restrained with a force constant of 1,000 kJ/mol during all simulations.

## Results

### Continuum Membrane Models Match Molecular Simulation

We first explored the ability of the continuum model to match deformations observed in simulations of ion and charged molecule permeation studies. We moved $K^+$ from the upper solution at $z = +30$ Å to the lower solution at $z = -30$ Å in 1 Å steps. At each step, we carried out a search algorithm to identify the contact values of the upper and lower leaflets and the membrane contact slope, or curvature, that minimized the total free energy in Eq. 1. The membrane was modeled as a large 800 Å radial patch with thickness and compression moduli derived for DPPC lipids (see Table 2), and in the flat, unstressed case it spans from +21.8 to −21.8 Å, centered at zero.

Four equilibrium snapshots of the ion at different positions along the permeation pathway are shown in Fig. 2a. The membrane adopts a low energy, large wavelength deformation to avoid the high energy electrostatic penalty of direct ion penetration into the hydrocarbon region. The far field boundaries are not shown, so the large scale deformation is not visible in each panel; therefore, the membrane shapes appear flat and unstrained only involving a global translation up or down along the $z$ axis. The insertion energy, $\Delta G_{tot}$, required to move the ion from bulk solution close to the center of the bilayer at $z = -1$ Å shown in the second panel of Fig. 2a, is nearly 0 kcal/mol. While physically intuitive, this result does not match the large 20–30 kcal/mol energies predicted for cation penetration into the core based on all-atom MD simulations (Tepper and Voth 2006; Li et al. 2012). Moreover, the membrane shape is completely different from published MD studies, and we hypothesized that this may be the result of MD simulations being performed on small patches of membrane (Tepper and Voth 2006; Leontiadou et al. 2007; MacCallum et al. 2007; Li et al. 2012).

To elucidate the source of these differences, we carried out our own MD simulations of a cation penetrating a bilayer using the coarse-grained MARTINI force field (Yesylevskyy et al. 2010) (Fig. 2b). MARTINI has been extensively used to simulate membrane distortions, ranging from TM and lipid fusion pores to large scale lipid rearrangement (Yoo et al. 2013; Marrink and Tieleman 2013). We constructed a small membrane composed of 128 DPPC lipids approximately 65 Å × 65 Å in area, comparable to patch sizes employed in all-atom MD simulations. Umbrella sampling was then used to harmonically restrain

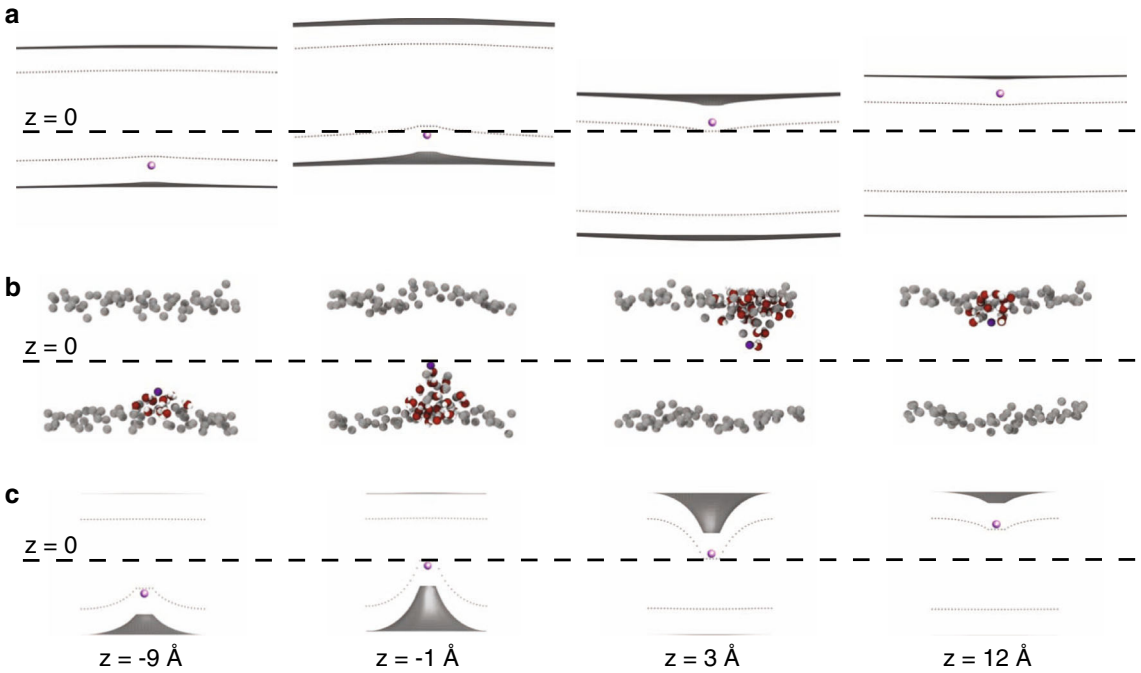


**Fig. 2** Continuum membrane bending is qualitatively similar to deformations observed in coarse-grained simulations. **a** Configurations from the continuum membrane bending model for a large patch of membrane with boundary conditions applied at 800 Å from the ion. Panels **a**–**c** all show four snapshots of a cation (*purple*) placed at −9, −1, +3, and +12 Å with respect to the center of mass of the membrane. In panels **a** and **c**, the *gray surfaces* are the membrane–water interfaces, which separate the head group region from aqueous solution. The interfaces between the head group region and the membrane core are shown as *gray dotted curves*. A search was carried out to identify the optimum membrane shape that minimizes the system energy for each ion position. The membrane undergoes large deflections in the $z$ direction to avoid penetration of the ion into the hydrocarbon core. These deflections are most pronounced when the ion is near the center at $z = -1$ and +3 Å causing shifts up and down, respectively. When the ion is at −9 and +12 Å the bilayer undergoes very little deflection from the flat, unstrained state. **b** Snapshots from a coarse-grained MD simulation of $Na^+$ penetrating a DPPC bilayer using the MARTINI forcefield. The membrane is approximately *square* with a side length of 65 Å, and it is composed of 128 DPPC lipids. The phosphate beads are *gray*, and penetrating waters are *red* and *white*. Starting with an identical flat, equilibrated bilayer, 71 independent umbrella sampling simulations were performed with the ion restrained at positions along the membrane normal. The small leaflet deformations occur at −9 and +12 Å, but large membrane bending occurs when the ion is near the center of the bilayer in the middle two snapshots. **c** Configurations from the continuum model for a small patch of membrane with a 19.5 Å radius. For this small patch, more similar in size to the system in panel **b**, the membrane is not able to adopt a low energy, large scale deformation to avoid penetration by the ion. The leaflet being penetrated bends sharply, while the opposite leaflet adopts a more gentle bend to relieve compression just as in the coarse-grained simulations in panel **b** (Color figure online)

the cation at positions along the $z$ axis ranging from −30 to +30 Å, with respect to the membrane COM, and representative snapshots were extracted from simulations at −9, −1, 3 and 12 Å (Fig. 2b). Consistent with past MD simulations, the coarse grained simulations reveal deep penetration of the ion into the membrane, which causes a severe deformation of the adjacent lipids. However, there was no large scale deflection of the membrane in the $\pm z$ direction, as observed in panel a, since the patch is not large enough to accommodate a long wavelength distortion given its small lateral extent.

Next, we carried out continuum calculations as in panel a, but with a much smaller patch size of radius 19.5 Å, comparable to the system size in the all-atom MD simulations of Li et al. (2012). Interestingly, the resulting minimized membrane configurations are now qualitatively similar to the MD simulations (compare Fig. 2b, c). The membrane is now too small to undergo a large deflection to keep the ion in the head group region, and instead the leaflets undergo bending to position the ion in the head group as it penetrates the bilayer. This result demonstrates that qualitative features of ion penetration into the membrane can be captured with a continuum model, and it highlights the importance of membrane size when exploring ion and small molecule permeation.

## Ion Free Energy Profiles from Continuum Model Match Profiles from Molecular Simulations

Next, we wanted to determine if our model produces energy values that are consistent with previous all-atom studies of ion permeation, and we wanted to understand the

role of membrane bending in this process. First, we computed the total free energy according to Eq. 1 for $K^+$ and $Cl^-$ movement across a non-deformable membrane in 1 Å steps (red and blue dashed lines in Fig. 3, respectively). The energy profile for an ion permeating a non-deformable bilayer exhibits a sharp increase as the ion leaves the high-dielectric head group region and then flattens out in the low-dielectric core between ±8 Å. The electrostatic cost of moving a charged solute into a low-dielectric region largely accounts for this effect, which is mediated slightly by the favorable change in the nonpolar energy arising from removing a solute from solution. Additionally, the anion is stabilized an additional ~20 kcal/mol compared to the cation because both ions experience the full effect of the +300 mV dipole potential. Importantly, these energy profiles do not match the "witch's hat" profiles produced by all-atom MD simulations, which show that the permeation profiles are sharply peaked near the bilayer center.

When we recompute the energy profile for ion permeation through a deformable membrane with DPPC-like bilayer properties, we see that the model reproduces sharply peaked energy profiles in qualitative agreement with MD (Tepper and Voth 2006; Khavrutskii et al. 2009; Li et al. 2012) (red and blue solid lines in Fig. 3). From the snapshots in Fig. 2c, we predicted that ion residence in the head group throughout the permeation process minimizes the electrostatic barrier to permeation while incurring an elastic cost for bending the membrane. Previously, we observed this interplay between electrostatics and elastostatics when we examined the insertion of arginine-containing helices into continuum elastic bilayers (Callenberg et al. 2012). Membrane bending lowers the energetic barrier to ion permeation by over 25 kcal/mol for $K^+$, revealing that the cost of bending the membrane is small relative to the electrostatic penalty of burying charge in the membrane.

Our model also stabilizes both cations and anions in the head group region at ±18 Å. Stabilization occurs because the head group dielectric is assumed to be the same as water, minimizing the electrostatic penalty, while desolvating the ions maximizes the nonpolar advantage of insertion. Another important feature of these profiles is that the energy difference between $K^+$ and $Cl^-$ is markedly reduced in the deformable model (solid) compared to the flat membrane profiles (dashed). As discussed in the last paragraph, selectivity arises from the positive dipole potential, which we model as two thin dipole sheets at the head group–hydrocarbon core interfaces. Since the ions remain largely in the head group region during penetration, they never fully cross this interface and hence never experience the full dipole potential. The fact that the ions never fully penetrate into the core of the continuum membrane is discussed in more detail in the "Discussion" section.

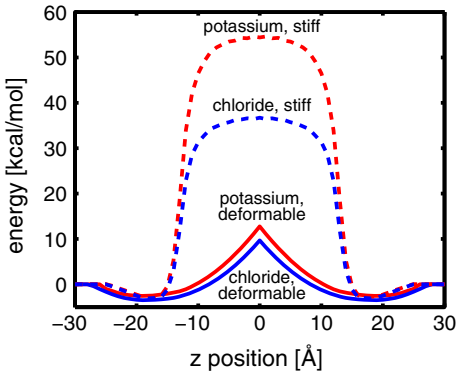


**Fig. 3** Free energy profiles along the transmembrane coordinate for a cation and an anion. We translated $K^+$ (*red curves*) or $Cl^-$ (*blue curves*) across the membrane in 1 Å steps with the ion initially positioned in bulk solvent approximately 6 Å from the membrane–water interface ($z = -30$ Å). *Dashed lines* correspond to calculations carried out on a stiff, unbending bilayer, while *solid lines* correspond to calculations carried out using the membrane bending model and minimizing the total energy in Eq. 1. Bending dramatically reduces the energy required to move ions into the center of the membrane by 12–30 kcal/mol. The membrane dipole reduces $Cl^-$ penetration by ~20 kcal/mol over $K^+$ in the non-deformable model (difference between *dashed curves*), but only by 2–3 kcal/mol in the membrane bending model (difference between *solid curves*) because ions never experience the full dipole potential in the later case (Color figure online)

## Permeation Barriers Increase with Increased Membrane Thickness

We next sought to examine membrane permeation in a variety of lipidic environments, which has implications for the analysis of small molecule permeability through different types of biological membranes. At present, the only systematic atomistic MD simulations exploring the influence of membrane thickness were carried out on $MGuanH^+$, which is a charged analog of the arginine side chain. We use those energy profiles here to qualitatively compare with our profiles for ion penetration. We translated a $K^+$ ion in 1 Å steps across membranes comparable to those used by Li et al. (2012) whose physical dimensions and material properties are listed in Table 2. The energy required to move the ion into the middle of the bilayer increases dramatically as the membrane thickness increases (Fig. 4a), which is in excellent agreement with the dependence observed in the energy profiles for $MGuanH^+$ permeation, shown in the inset. Both our continuum results and the all-atom MD are in qualitative agreement with the experimental finding that ion permeability values drastically increase with bilayer thickness (Paula et al. 1996). The absolute value of the energies reported at the membrane center are different for $K^+$ and $MGuanH^+$, which is

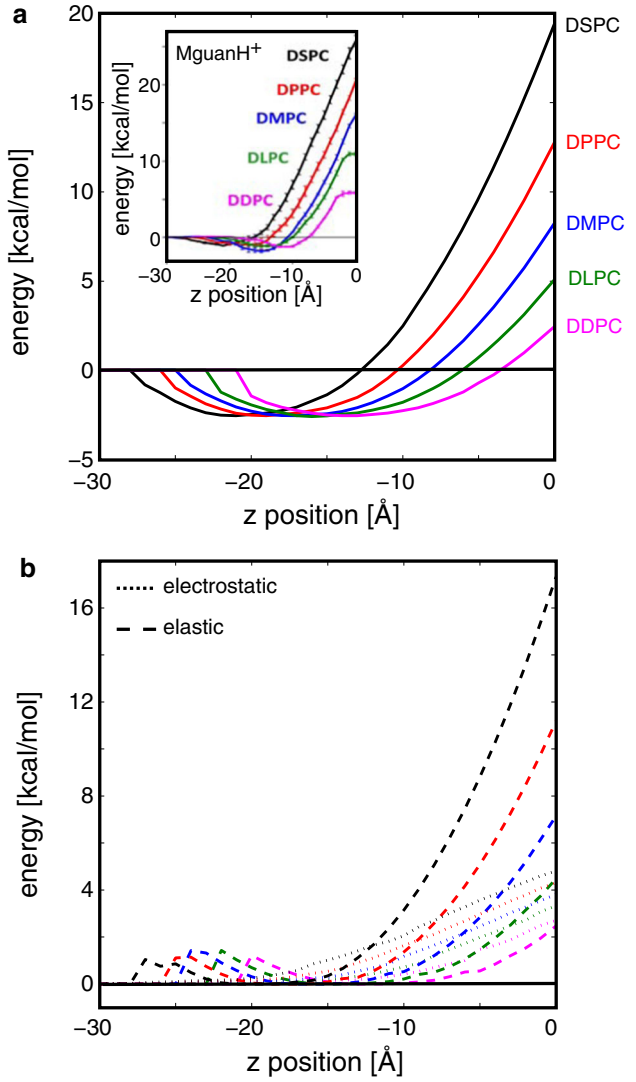


**Fig. 4** Free energy profiles for $K^+$ penetration into bilayers of different thicknesses. **a** For all thicknesses, the ion is stabilized as it enters the head group region, but rises to a sharp-peak at the membrane center. The penetration energy increases with membrane thickness with values at the center ranging from 3 to 18 kcal/mol. The *inset* shows similar free energy profiles obtained from atomistic MD simulations carried out on the positively charged arginine side chain analogue, $MGuanH^+$ (Li et al. 2012). The equilibrium thickness ($L_0$) and bending modulus ($K_c$) were increased to match the known properties of lipids being modeled, and values are given in Table 2. The compression modulus ($K_a$) was held constant since it is thought to be independent of the hydrophobic thickness. In all cases, $L_0$ for each lipid type is similar between the MD simulations and continuum model except for DSPC, as discussed in the "Methods" section. **b** Elastic (*dashed*) and electrostatic (*dotted*) energy contributions to the insertion energy values in panel **a**. The *color scheme* is the same as panel **a**. As the ion first enters the head group between −28 and −22 Å, depending on the lipid type, there is a small jump in the bending energy due to the bilayer bending up to meet the ion. Near the *center* of the bilayer, the elastic energy term dominates for *thicker* bilayers, but the elastic and electrostatic components are similar for *thinner* bilayers. The nonpolar energy term is not shown since it is relatively simple: it decreases by a set amount as the ion penetrates the head group, and then it remains flat

not surprising given their chemical differences. Also, the $MGuanH^+$ profiles plateau near $z = 0$ Å for thinner membranes, DDPC and DLPC, which is not observed in our continuum profiles and is likely due to membrane reorganization as discussed later.

We also determined the individual energy contributions from the elastic, electrostatic, and nonpolar components of the model (Fig. 4b). Interestingly, while the elastic component of the free energy increases quadratically with increasing bilayer thickness, the electrostatic and nonpolar contributions depend very weakly on bilayer thickness (Fig. 4b). Likewise, only the elastic component of the free energy is affected by changes in lipid patch size (data not shown), a result that is most likely a direct consequence of our elastic treatment of the membrane. Thus, the increase in energy observed in Fig. 4a with increasing bilayer thickness is a direct consequence of the ion penetrating a longer distance to reach the center of thicker membranes.

## Membrane Patch Size Influences Binding Energies

Our initial observation in Fig. 2a was that calculations on large membrane systems do not match observed deformations from MD simulations, and simply restricting the membrane size in our continuum model allowed us to accurately match results from MD (Fig. 2c). We wanted to ask the converse question; that is, do MD simulations carried out on large membranes provide qualitatively and quantitatively different answers than simulations performed on small membranes? To answer this question, we again carried out MARTINI simulations, but this time on a protein segment known to bind membranes: helix 2 from the RAH domain of *T. gondii* ROP5 (Reese and Boothroyd 2009; El Hajj et al. 2007). We hypothesized that the simulation of a small, known membrane binding segment would elicit a more detectable dependence on membrane patch size than the simulation of a single ion, which is true based on our CG simulations of ions (data not shown). ROP5 is a rhoptry protein secreted by the human pathogen *T. gondii* during infection of a host cell and is a very potent virulence factor in this organism (Reese et al. 2011; Behnke et al. 2011). Its binding to the parasitophorous vacuole membrane (PVM), which surrounds the parasite, is driven by a specific RAH domain consisting of three putative alpha-helices (Reese and Boothroyd 2009). The RAH domain is both necessary and sufficient for membrane binding, and deletion of helix 2 of the RAH domain most effectively reduces ROP5 binding to the PVM (Reese and Boothroyd 2009), leading to the hypothesis that helix 2 has the highest binding affinity to the membrane. It is postulated, but not known, that the RAH helices of ROP5 bind interfacially to the PVM (Reese and Boothroyd 2009).

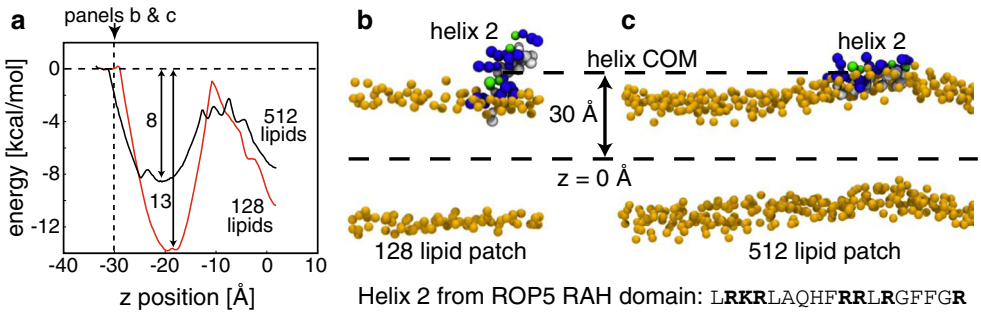


**Fig. 5** Free energy of ROP5 RAH helix 2 binding to a membrane. **a** The potential of mean force (PMF) for ROP5 RAH helix 2 translated from the *lower* bath into the *center* of the bilayer. The PMFs are flat in water, but exhibit a sharp downward slope at −32 Å (512 patch, *black curve*) and −28 Å (128 patch, *red curve*) when the membrane starts to bend to interact with the helix. The large patch is able to bend to reach the helix before the small patch leading to robust differences between the two PMFs. The interfacial region near −20 Å is the most stable position for both simulations, but the binding is predicted to be 5 kcal/mol more stable for the small patch than the large patch. The interface between the head group and aqueous environment in the unstrained membrane is indicated by the *vertical dashed line*. **b**, **c** Significant membrane deformations are observed in the large coarse-grained system, but not the small system. When helix 2 from the ROP5 protein is restrained at ±30, +30 Åis shown here, from the *center* of a DPPC bilayer, a *large* membrane patch is able to undergo a large scale conformational change to allow the helix to go completely interfacial (**c**), while the *small* patch is unable to accommodate such a bending mode (**b**). Only the distance from the helix COM to the membrane COM are restrained, and the orientation of the helix is free to rotate. Without membrane bending, the distance restraint prevents the entire helix from embedding in the membrane interface (**b**). These differences in system size give rise to differences in the energetics of helix association with the membrane in panel **a** (Color figure online)

The binding energy for ROP5 helix 2 is reported in Fig. 5a for both a small membrane patch of 128 lipids (red curve) and a large membrane patch with 512 lipids (black curve). As expected based on its amphipathic character (see bottom of Fig. 5 for sequence), the helix is most stable at the membrane–water interface (−20 Å). It adopts a conformation with the hydrophobic face buried in the membrane core and the arginine residues exposed to water, regardless of lipid patch size (snapshots not shown). This configuration is consistent with what has been proposed for the ROP5 RAH domain helices (Reese and Boothroyd 2009). Interestingly, the free energy curves are not identical for these two systems. While the energy barriers at the center of the bilayer are nearly identical, the shape of the PMFs are quite different, leading to different estimates of the interfacial binding energy, −8 versus −13 kcal/mol, for small and large patches, respectively (Fig. 5a). We observe that when a small number of lipids are simulated with the helix restrained at ±30 Å from the membrane center, large scale membrane bending does not occur, and the helix remains largely solvated in water (Fig. 5b). The distance restraint prevents the helix from getting closer to the membrane and going interfacial, while the small size of the membrane patch makes it prohibitively difficult to bend and fully contact the helix. However, simulations of the same situation with the larger patch size show a large scale deformation of the bilayer that embeds the hydrophobic residues in the membrane (Fig. 5c). We performed three additional simulations with different random seeds for each system and found this difference in membrane behavior was consistent; the large patch always bent, while the smaller patch never exhibited large scale bending during the length of the entire simulation. The behavior is in exact agreement with our continuum model shown in Fig. 2a in which the membrane undergoes large scale deformations to minimize the energy of the system. In small patch size simulations, it is not possible for the membrane to undergo such large scale deformations, and the results are necessarily higher energy compared to the larger systems.

## Discussion

Our continuum model produces shapes (Fig. 2b, c) and energetics (Fig. 4a) that are qualitatively consistent with fully atomistic and coarse-grained simulations of ion penetration into membranes. This connection is encouraging since ion, ionophore and peptide permeation across membranes is of extreme interest from both a basic biological stand point and a pharmacological perspective. Computational approaches to understanding these phenomena are needed to gain atomic level insight and provide predictive power. One advantage of a continuum model is that the reduction of the system size, by treating the membrane and water as a continuum, leads to energy calculations that are thousands of times faster than corresponding atomistic simulations (Callenberg et al. 2012). Another benefit of our approach is that it is quite easy to determine the contribution of each energy term in the model to the total energy. The decomposition in Fig. 4b shows that the dependence of insertion energy on membrane thickness is largely described by the increase in elastic energy required to bend

thicker membranes. Such a decomposition can be difficult for atomistic simulations because it requires averaging over many configurations and macroscopic energies such as elasticity are not easily computed.

Calculations in Fig. 4a show that both cations and anions are stabilized in the head group region, which is in agreement with recent experiments (Knecht and Klasczyk 2013). This property is not captured by most all-atom MD simulations (Tepper and Voth 2006; Khavrutskii et al. 2009), but it has been reported that $Cl^-$ binds to the head group using the GROMACS force field, albeit more weakly than $Na^+$ (Pandit et al. 2003). Furthermore, it has been argued that stabilization of anions in the PC head group may not be possible with classic MD, but may require a polarizable force field (Knecht and Klasczyk 2013; Woolf 2013). Such calculations are even more computationally demanding than classic all-atom MD, again highlighting the usefulness of our continuum approach, which already reproduces the correct anion/cation stabilization, and can be further tuned to match experiment. Additionally, our model suggests that ions that have moved into the bilayer do not sense the full strength of the membrane dipole potential because they remain in the head group region. This was also observed by Vorobyov and colleagues who used all-atom MD to show a similar result for $MGuanH^+$ permeation (Vorobyov et al. 2010).

Unfortunately, our model does not lend much insight into the nature of the transition state for passive ion permeation. The presence of the ion induces deformations in the membrane shape, which supports the ion-induced defect model (Li et al. 2012). However, when the ion is at the center of the membrane, symmetry is broken depending on which side the ion originated (Fig. 6). The left hand snapshot shows the ion at the center of the membrane, where it still remains in the lower head group, separated from the upper leaflet by the hydrophobic core. Moving the ion 1 Å farther produces a snap through bifurcation in which the ion becomes localized in the upper leaflet (right). Thus, our model does not capture the configurations in which the ion is either exposed to the hydrophobic core (solubility-diffusion model) or in which a pore defect is created through the bilayer (transient pore formation model). Pore formation involves a topological change in the membrane, which is not possible in our current elastic energy formulation. As we continue to formulate more accurate continuum models of the membrane, we may be able to incorporate topological changes, which would allow us to return to the question of permeation and predicting permeabilities with our model.

Perhaps our most important observation is that computed energy profiles for ion and peptide association with the membrane depend on the size of the membrane patch. Only by matching lipid patch size could we achieve

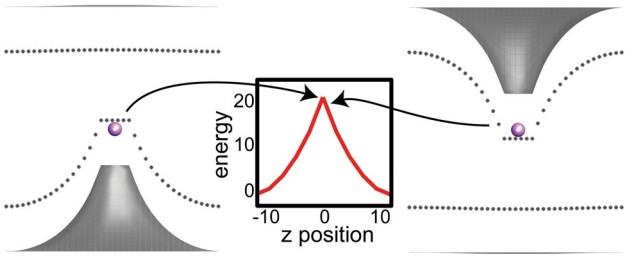


**Fig. 6** The continuum model fails to reproduce the transition state for ion permeation. Membrane configurations from the continuum model for a $K^+$ at the center of the membrane (*left*) and just to the right of the membrane center (*right*). The relevant portion of the energy profile from Fig. 3 is shown in the middle

consistency between continuum and coarse-grained models. Our continuum model shows that if the membrane patch is large enough, low energy, long wavelength deformations in the bilayer allow for protein–membrane interactions over long distances (Callenberg et al. 2012), and this is highlighted in our qualitative, coarse grained simulations of ROP5 (Fig. 5a). The underlying free energy profiles are quite different for the small patch and the large patch, leading to considerable variation in the predicted membrane binding energies (−13 vs. −8 kcal/mol, respectively). Our continuum model explains why the larger patch size is able to interact with the peptide held farther away from the membrane center, but it does not explain why the small patch binds so much tighter. We hypothesize that the peptide suppresses entropic fluctuations in the large membrane, which are not present in the small patch, but we have no calculations to support this notion. Moreover, it is not clear which simulation setup is most appropriate for comparing with experimental binding energy values. One way to remove the dependence on patch size is to define the membrane COM using a small number of lipid molecules within a cutoff radius of the permeating molecule, as was done by Bennett and Tieleman (2011) for all-atom simulations on $MGuanH^+$. This definition selects higher energy configurations, but it also uncouples the long wavelength behavior of the membrane to the local changes that accompany permeation. Nonetheless, while the application of a restraining potential to a large bilayer represents one way to overcome size differences among models, it is also prohibitive for the study of large scale membrane deformations. Importantly, our results complement the recent findings of the Patel group, which used all-atom simulations to demonstrate that $MGuanH^+$ permeation through a large lipid patch incurs a small energetic cost relative to permeation through a small patch (Hu et al. 2013)—exactly what we found for $K^+$ in the "Continuum Membrane Models Match Molecular Simulation" section.

The idea of membrane patch size as a determinant of deformation energy has implications in other biological contexts as well. In one study, continuum and coarse-grained models of membrane fusion pores predicted nearly identical membrane configurations and curvatures when the lateral dimensions of the simulated bilayers were matched in both systems (Yoo et al. 2013). Increasing patch size dramatically changed the shape of bowing during energy minimization of the continuum model, suggesting that the membrane area available during fusion directly affects the energetics of pore formation. With this in mind, the importance of patch size may have been overlooked in previous studies of membrane inclusion induced deformations. In one study, the authors concluded that a range of inclusion radii and monolayer thicknesses led to only small changes in the induced membrane curvature during the insertion of a cylinder into a continuum membrane (Campelo et al. 2008). However, the significance of this observation was assessed for only a single lateral dimension of the membrane. For other patch sizes, our data suggest that as dimensions increase, strain will spread out over the lateral dimensions of the membrane, reducing the elastic energy and changing the curvature of the deformation. Similarly, the size of the membrane patch available for bending could alter, for example, the affinity of BAR domain proteins with the membrane and induce curvature that aids fusion pore formation (Zimmerberg and Kozlov 2005).

While our continuum model accurately describes large scale deformations, difficult to capture via molecular simulations, it does not capture small length scale changes at the single lipid level. Kim et al. (2012) recently described the membrane deformation profile around the membrane spanning antibiotic peptide gramicidin A. They showed that the membrane surface undergoes non-monotonic changes in height in the first few lipid shells surrounding the peptide, and our experience leads us to agree with their conclusion that such solutions are not possible given the class of elastic models we are using. The impact of these undulations on membrane–protein function and system energetics must be further explored, and it may take more sophisticated continuum models to describe membrane structure at this level of detail. Given these considerations, we believe that a multi-pronged computational approach to membrane permeation is needed to describe both large scale deformations with continuum models and small length scale interactions with all-atom MD. For instance, the membrane geometry could first be optimized around a protein with the continuum model and then the shape could subsequently be used as a constraint for packing all-atom lipids into the system. The Weinstein Lab has already implemented a method that combines both all-atom MD and continuum methods to better understand the energetics of their membrane–protein systems (Mondal et al. 2011). Similarly, the Jacobson Laboratory has created a hybrid approach that uses molecular simulation together with simple solubility-diffusion models through flat membranes to rapidly assess neutral cyclic peptide and small molecule membrane permeability (Rezai et al. 2006a, b; Leung et al. 2012). The incorporation of our membrane bending model into this latter framework may make it possible to explore the permeation of charged and highly polar molecules and peptides, offering opportunities for high-throughput design and screening of novel membrane permeable compounds.

**Acknowledgments** We would like to thank Nwamaka Onyeozili, Siyu Xiao, Mary Krawczak, and Shuchang Liu for their assistance in setting up and running initial variations of the coarse-grained MD simulations. We also thank Frank Marcoline for help implementing the dipole potential, and John Rosenberg, Daniel Zuckerman, Patrick Van der Wel, Joshua Adelman and Charles Wolgemuth for enlightening discussions. Naomi R. Latorraca was supported by an Undergraduate Research Fellowship from the Howard Hughes Medical Institute, and this work was supported by an NSF CAREER Award (MCB-0722724) to Michael Grabe and a Pew Scholarship in the Biomedical Sciences to Jon P. Boyle. We dedicate this work to Harold Lecar, a deep scholar, incredible teacher and good friend.

## References

Baker NA, Sept D, Joseph S, Holst MJ, McCammon JA (2001) Electrostatics of nanosystems: application to microtubules and the ribosome. Proc Natl Acad Sci USA 98(18):10037–10041

Behnke MS, Khan A, Wootton JC, Dubey JP, Tang K, Sibley LD (2011) Virulence differences in *Toxoplasma* mediated by amplification of a family of polymorphic pseudokinases. Proc Natl Acad Sci USA 108(23):9631–9636

Bennett WD, Tieleman DP (2011) Water defect and pore formation in atomistic and coarse-grained lipid membranes: pushing the limits of coarse graining. J Chem Theory Comput 7(9):2981–2988

Berendsen HJC, Postma JPM, van Gunsteren WF, DiNola A, Haak JR (1984) Molecular dynamics with coupling to an external bath. J Chem Phys 81(8):3684. doi:10.1063/1.448118

Bond PJ, Wee CL, Sansom MS (2008) Coarse-grained molecular dynamics simulations of the energetics of helix insertion into a lipid bilayer. Biochemistry 47(43):11321–11331

Budin I, Szostak JW (2011) Physical effects underlying the transition from primitive to modern cell membranes. Proc Natl Acad Sci USA 108(13):5249–5254

Callenberg KM, Choudhary OP, Gabriel L, Gohara DW, Baker NA, Grabe M (2010) APBSmem: a graphical interface for electrostatic calculations at the membrane. PloS ONE 5(9):e12722

Callenberg KM, Latorraca NR, Grabe M (2012) Membrane bending is critical for the stability of voltage sensor segments in the membrane. J Gen Physiol 140(1):55–68. doi:10.1085/jgp.201110766

Campelo F, McMahon HT, Kozlov MM (2008) The hydrophobic insertion mechanism of membrane curvature generation by proteins. Biophys J 95(5):2325–2339

Choe S, Hecht KA, Grabe M (2008) A continuum method for determining membrane protein insertion energies and the problem of charged residues. J Gen Physiol 131(6):563–573. doi:10.1085/jgp.200809959

de Gennes P (1969) Conjectures sur l'etat smectique. J Phys Colloq 30(C4):C4–C65

Dilger JP, McLaughlin S, McIntosh TJ, Simon SA et al (1979) The dielectric constant of phospholipid bilayers and the permeability of membranes to ions. Science 206(4423):1196

Dorairaj S, Allen TW (2007) On the thermodynamic stability of a charged arginine side chain in a transmembrane helix. Proc Natl Acad Sci USA 104(12):4943–4948. doi:10.1073/pnas.0610470104

El Hajj H, Lebrun M, Fourmaux MN, Vial H, Dubremetz JF (2007) Inverted topology of the *Toxoplasma gondii* ROP5 rhoptry protein provides new insights into the association of the ROP2 protein family with the parasitophorous vacuole membrane. Cell Microbiol 9(1):54–64

Finkelstein A (1987) Water movement through lipid bilayers, pores, and plasma membranes: theory and reality. Wiley–Interscience, New York

Harroun TA, Heller WT, Weiss TM, Yang L, Huang HW (1999) Experimental evidence for hydrophobic matching and membrane-mediated interactions in lipid bilayers containing gramicidin. Biophys J 76(2):937–945

Helfrich W (1973) Elastic properties of lipid bilayers: theory and possible experiments. Z Naturforsch Teil C Biochem Biophys Biol Virol 28(11):693

Helm C, Möhwald H, Kjaer K, Als-Nielsen J (1987) Phospholipid monolayer density distribution perpendicular to the water surface. A synchrotron X-ray reflectivity study. Europhys Lett 4(6):697

Hess B, Kutzner C, van der Spoel D, Lindahl E (2008) GROMACS 4: algorithms for highly efficient, load-balanced, and scalable molecular simulation. J Chem Theory Comput 4(3):435–447. doi:10.1021/ct700301q

Hessa T, Kim H, Bihlmaier K, Lundin C, Boekel J, Andersson H, Nilsson I, White S, Von Heijne G (2005) Recognition of transmembrane helices by the endoplasmic reticulum translocon. Nature 433(7024):377–381. doi:10.1038/nature03216

Hu Y, Ou S, Patel S (2013) Free energetics of arginine permeation into model DMPC lipid bilayers: coupling of effective counter-ion concentration and lateral bilayer dimensions. J Phys Chem B 117(39):11641–11653. doi:10.1021/jp404829y

Hub JS, Groot BLD, Spoel DVD (2010) g_wham: a free weighted histogram analysis implementation including robust error and autocorrelation estimates. J Chem Theory Comput 6:3713–3720

Humphrey W, Dalke A, Schulten K (1996) VMD: visual molecular dynamics. J Mol Graph 14(1):33–38. doi:10.1016/0263-7855(96)00018-5

Kandasamy SK, Larson RG (2006) Cation and anion transport through hydrophilic pores in lipid bilayers. J Chem Phys 125:074901

Khavrutskii IV, Gorfe AA, Lu B, McCammon JA (2009) Free energy for the permeation of $Na^{(+)}$ and $Cl^{(-)}$ ions and their ion-pair through a zwitterionic dimyristoyl phosphatidylcholine lipid bilayer by umbrella integration with harmonic Fourier beads. J Am Chem Soc 131(5):1706–1716. doi: 10.1021/ja8081704

Kim T, Lee KI, Morris P, Pastor RW, Andersen OS, Im W (2012) Influence of hydrophobic mismatch on structures and dynamics of gramicidin A and lipid bilayers. Biophys J 102(7):1551–1560

Knecht V, Klasczyk B (2013) Specific binding of chloride ions to lipid vesicles and implications at molecular scale. Biophys J 104(4):818–824

Kumar S, Bouzida D, Swendsen R, Kollman P, Rosenberg J (1992) The weighted histogram analysis method for free-energy calculations on biomolecules. J Comput Chem 13(8):1011–1021

Leontiadou H, Mark AE, Marrink SJ (2007) Ion transport across transmembrane pores. Biophys J 92(12):4209–4215. doi:10.1529/biophysj.106.101295

Leung SS, Mijalkovic J, Borrelli K, Jacobson MP (2012) Testing physical models of passive membrane permeation. J Chem Inf Model 52(6):1621–1636

Lewis BA, Engelman DM (1983) Lipid bilayer thickness varies linearly with acyl chain length in fluid phosphatidylcholine vesicles. J Mol Biol 166(2):211–217

Li LB, Vorobyov I, Allen TW (1818) The role of membrane thickness in charged protein–lipid interactions. Biochim Biophys Acta Biomembr 1818(2):135–145. doi:10.1016/j.bbamem.2011.10.026

MacCallum JL, Bennett WFD, Tieleman DP (2007) Partitioning of amino acid side chains into lipid bilayers: results from computer simulations and comparison to experiment. J Gen Physiol 129(5):371–377. doi:10.1085/jgp.200709745

Mansy SS, Szostak JW (2008) Thermostability of model protocell membranes. Proc Natl Acad Sci USA 105(36):13351–13355

Marrink SJ, Tieleman DP (2013) Perspective on the MARTINI model. Chem Soc Rev 42:6801–6822

Marrink SJ, de Vries AH, Tieleman DP (2009) Lipids on the move: simulations of membrane pores, domains, stalks and curves. Biochim Biophys Acta Biomembr 1788(1):149–168

Mills JC, Stone NL, Erhardt J, Pittman RN (1998) Apoptotic membrane blebbing is regulated by myosin light chain phosphorylation. J Cell Biol 140(3):627–636

Mondal S, Khelashvili G, Shan J, Andersen OS, Weinstein H (2011) Quantitative modeling of membrane deformations by multihelical membrane proteins: application to G-protein coupled receptors. Biophys J 101(9):2092–2101

Pandit SA, Bostick D, Berkowitz ML (2003) Molecular dynamics simulation of a dipalmitoylphosphatidylcholine bilayer with NaCl. Biophys J 84(6):3743

Parsegian A (1969) Energy of an ion crossing a low dielectric membrane: solutions to four relevant electrostatic problems. Nature 221(5183):844

Paula S, Volkov A, Van Hoek A, Haines T, Deamer D (1996) Permeation of protons, potassium ions, and small polar molecules through phospholipid bilayers as a function of membrane thickness. Biophys J 70(1):339–348

Paula S, Volkov A, Deamer D (1998) Permeation of halide anions through phospholipid bilayers occurs by the solubility-diffusion mechanism. Biophys J 74(1):319–327. doi:10.1016/S0006-3495(98)77789-6

Powell MJD (1964) An efficient method for finding the minimum of a function of several variables without calculating derivatives. Comput J 7(2):155–162. doi:10.1093/comjnl/7.2.155

Rawicz W, Olbrich KC, McIntosh T, Needham D, Evans E (2000) Effect of chain length and unsaturation on elasticity of lipid bilayers. Biophys J 79(1):328–339. doi:10.1016/S0006-3495(00)76295-3

Reese ML, Boothroyd JC (2009) A helical membrane-binding domain targets the *Toxoplasma* ROP2 family to the parasitophorous vacuole. Traffic 10(10):1458–1470

Reese ML, Zeiner GM, Saeij JP, Boothroyd JC, Boyle JP (2011) Polymorphic family of injected pseudokinases is paramount in *Toxoplasma* virulence. Proc Natl Acad Sci USA 108(23):9625–9630

Rezai T, Bock JE, Zhou MV, Kalyanaraman C, Lokey RS, Jacobson MP (2006a) Conformational flexibility, internal hydrogen bonding, and passive membrane permeability: successful in silico prediction of the relative permeabilities of cyclic peptides. J Am Chem Soc 128(43):14073–14080

Rezai T, Yu B, Millhauser GL, Jacobson MP, Lokey RS (2006b) Testing the conformational hypothesis of passive membrane permeability using synthetic cyclic peptide diastereomers. J Am Chem Soc 128(8):2510–2511

Shannon R (1976) Revised effective ionic radii and systematic studies of interatomic distances in halides and chalcogenides. Acta Crystallogr A 32(5):751–767

Shrake A, Rupley J (1973) Environment and exposure to solvent of protein atoms, lysozyme and insulin. J Mol Biol 79(2):351–371

Sitkoff D, Sharp KA, Honig B (1994) Accurate calculation of hydration free energies using macroscopic solvent models. J Phys Chem 98(7):1978–1988

Vepper H, Voth G (2006) Mechanisms of passive ion permeation through lipid bilayers: insights from simulation. J Phys Chem B 110(42):21327–21337

Tieleman DP, Marrink SJ (2006) Lipids out of equilibrium: energetics of desorption and pore mediated flip-flop. J Am Chem Soc 128(38):12462–12467

Vorobyov I, Bekker B, Allen TW (2010) Electrostatics of deformable lipid membranes. Biophys J 98(12):2904–2913

Wang L, Bose PS, Sigworth FJ (2006) Using cryo-EM to measure the dipole potential of a lipid membrane. Proc Natl Acad Sci USA 103(49):18528–18533

Wee CL, Chetwynd A, Sansom MS (2011) Membrane insertion of a voltage sensor helix. Biophys J 100(2):410

Woolf TB (2013) A tale of two ions and their membrane interactions: clearly the same or clearly different? Biophys J 104(4):746–747

Yesylevskyy SO, Schäfer LV, Sengupta D, Marrink SJ (2010) Polarizable water model for the coarse-grained MARTINI force field. PLoS Comput Biol 6(6):e1000810. doi:10.1371/journal.pcbi.1000810

Yoo J, Jackson MB, Cui Q (2013) A comparison of coarse-grained and continuum models for membrane bending in lipid bilayer fusion pores. Biophys J 104(4):841–852

Zimmerberg J, Kozlov MM (2005) How proteins produce cellular membrane curvature. Nat Rev Mol Cell Biol 7(1):9–19